Experimental Study on the Effect of a Strong Negative Pressure Gradient on a Shear-driven Liquid Fuel Film

P. Schober, J. Ebner, O. Schäfer, S. Wittig

Lehrstuhl und Institut für Thermische Strömungsmaschinen
Universität Karlsruhe (TH)
76128 Karlsruhe, Germany

Shear-driven liquid wall films play a major role in the fuel preparation process in advanced prefilming gas turbine combustor nozzles. Advanced two-phase flow CFD-codes have been identified as a valuable tool in the design and the optimisation process of these components. For the CFD calculations, it is assumed that the wavy liquid film propagates with a time averaged local film thickness $\bar{h}_f$. The wavy surface structure and its interaction with the gaseous phase is described via a sand grain roughness approach. For a full description of the liquid film motion, the shear-stress τ at the air/liquid interface, the equivalent sand grain roughness k_s and the mean film thickness $\bar{h}_f$ have to be determined. To develop a correlation for the roughness effect of the wavy film surface on the driving co-current accelerated air flow, numerous measurements in an atmospheric wind tunnel have been performed. Additional experiments in a geometry typical of the technical application at elevated pressures allow a validation of this correlation.

1. Introduction

Shear-driven liquid wall films play a major role in the fuel preparation process in advanced prefilming aviation gas turbine combustor nozzles. The performance of the fuel preparation components influences strongly the pollutant emissions and the stability of the combustion process. A common design solution are prefilming airblast atomisers (Fig. 1(a)). In this design, the liquid fuel is spread on the inner surface of a convergent nozzle. The liquid film propagates towards the atomiser edge, driven by the air flow, which is accelerated due to the nozzle geometry. At the atomisation edge the liquid film is exposed to air flows from both sides with high relative velocities. Because of the strong aerodynamic forces, the liquid film disintegrates in several steps to a fine spray of small droplets.

To simulate the interaction of the liquid film and the air flow within the complex geometry of a technical atomiser, a simplified model for the coupling of both phases is needed. The CFD film flow module of the Institut für Thermische Strömungsmaschinen (ITS) assumes, that the liquid film propagates with a time averaged local film thickness $\bar{h}_f$ [1]. The wavy surface structure of the liquid film and its influence on the gaseous phase is described via a sand grain roughness approach [2]. A shape factor Ψ (Eq. 1), which has to be determined from experimental results, takes account of the varying influence of the film surface depending on its structure and its mean film height $\bar{h}_f$. The shape factor is influenced by the present pressure gradient dp/dx, the shear-stress τ at the gas/liquid interphase and the physical properties σ_f, ρ_f, ν_f of the liquid, according to

$$\Psi(\bar{h}_f, dp/dx, \tau, \sigma_f, \rho_f, \nu_f) = \frac{k_s}{2\bar{h}_f}. \tag{1}$$

To derive the shape factor Ψ from experimental data, the equivalent sand grain roughness k_s and

the mean film thickness $\bar{h}_f$ as well as the driving shear-stress τ at the air/liquid interface have to be determined. Since a direct measurement of the shear-stress at air/liquid interface seems to be impossible, the values are calculated in a post-processing by matching the air velocity profiles above the liquid film to a modified wall function.

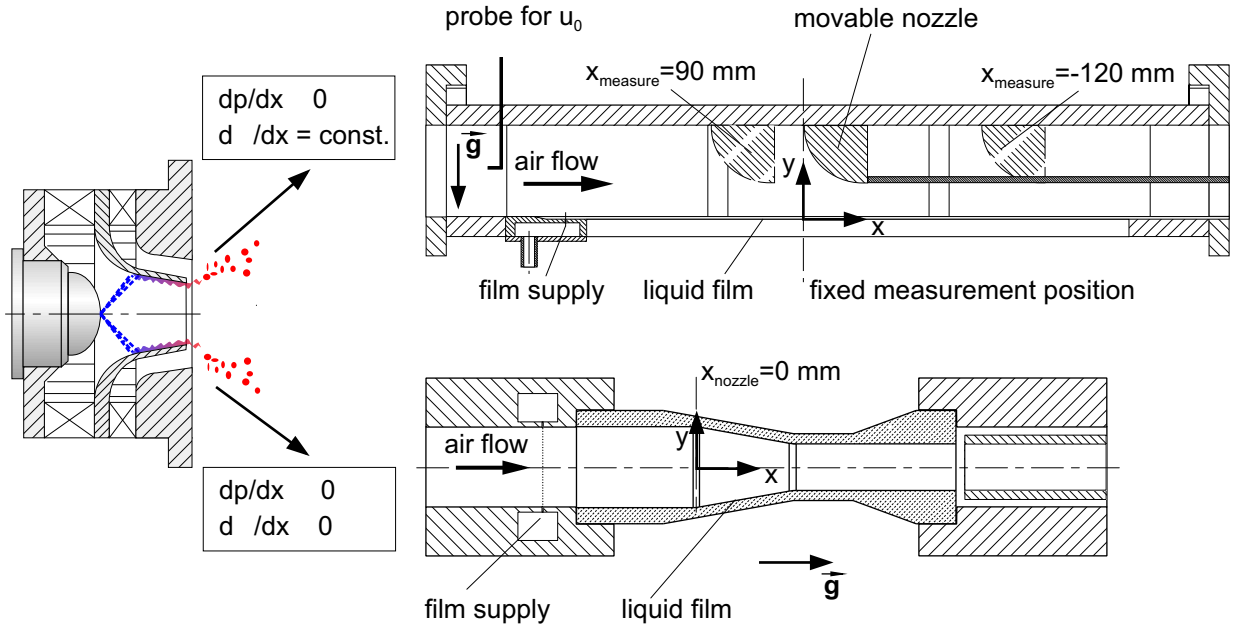

(a) Airblast atomiser **(b)** Test sections derived from the original geometry

Fig. 1 Simplified model geometries derived from the technical application

Various previous investigations focused on non-accelerated film flow on plane surfaces at atmospheric pressure have led to a well validated CFD tool for those cases. In opposite to that, the flow condition in the prefilming area of an airblast atomiser (Fig. 1(a)) are far more complex. Beside the elevated air pressure, two additional strong effects due to the atomiser geometry can be identified. In most of the cases the geometry of the atomiser causes an acceleration of the air flow to improve the fuel atomisation, resulting in a strong negative pressure gradient dp/dx. To investigate exclusively the effect of the pressure gradient, a first test rig with film flow on a plane surface with an accelerated driving air flow was designed (Fig. 1(b)(top)). At this test rig with excellent optical access to both the air and the liquid flow a correlation for the shape factor Ψ in terms of the variables in Eq. 1 is developed. The second effect caused by a convergent film flow surface is the changing of the local film load $\Lambda = \dot{V}/b$. Since this effect can only be investigated in an axially symmetric geometry, a second test rig was set-up. The geometry investigated at this rig is close to the one found in common airblast atomisers. The disadvantage of the axially symmetric geometries is the lack of an optical access to the air flow above the liquid film. This restricts the experimental investigation to the measurement of the film thickness, which allow a validation of the deduced correlations with the help of CFD calculations (see [3]).

2. Test facilities for film flow experiments

A sketch of the test section used to investigate the effect of an accelerating air flow on the film roughness and therefore on the shape factor Ψ respectively is shown in Fig. 1(b) (top). The flow duct has a rectangular cross section with a width of 190 mm and a inlet height of $H_{in} = 90$ mm.

Glass windows in the film propagation surface as well as the side and the top walls offer an excellent optical access. The air flow above the liquid film is accelerated via a movable nozzle opposite the film propagation surface. The nozzle with a radius of $r = 60\ mm$ reduces the height of the duct to $H_{out} = 30.0\ mm$. The liquid film propagates along the bottom of the duct. A 1.5 *mm* deep and 80 *mm* wide indentation confines the lateral spread of the liquid film and thus the influence of side wall effects of the gas flow on the liquid film. To avoid displacement while traversing along the film propagation surface, the measurement devices are fixed at the center of the test section. The nozzle moved via a linear stage permits measurements in a range from $x_{measure} = -120\ mm$ to $x_{measure} = 90\ mm$. Since the travelling range of the nozzle is short compared to the length of the flow channel upstream the nozzle, the conditions of the boundary layer within the nozzle are not depending on the nozzle position. A suction side blower permits air flow velocities up to $u_{air,\ in} = 25\ m/s$ at the inlet of the test section.

Figure 1(b) (bottom) shows the test section for the high pressure film flow experiments in a more complex geometry. The test section is made out of acrylic glass to achieve an optical access to the film flow inside the duct. In this paper measurements in a convergent nozzle are presented. The inlet diameter of $d_{in} = 40\ mm$ is reduced via a nozzle with a half-angle of 10° to $d_{out} = 23\ mm$. At the beginning and the end of the nozzle a round with a radius of $r = 18\ mm$ smoothes the junctions. To avoid an uneven distribution of the film liquid along the nozzle diameter due to gravity, the test rig is assembled in an vertical arrangement. The liquid film is supplied to the inner surface via 90 holes with an diameter of $d = 0.5\ mm$. By the pressurised air supply, pressures of up to $p_{in} = 0.8\ MPa$ and inlet velocities of up to $u_{air,\ in} = 30\ m/s$ can be achieved.

In both test rigs a controlled liquid pump allows the variation of the film load between $\Lambda = \dot{V}_{film}/b = 0.1$ and $1.0\ cm^2/s$. The physical properties of the film liquid influencing its interaction with the driving gas flow are the density, the viscosity and the surface tension of the fluid. For the film flow experiments a liquid is utilised which has physical properties similar to those of kerosene at $80^\circ C$. At ambient temperature, at which all experiments are performed, the properties of the film fluid are $\rho_f = 781\ kg/m^3, \nu_f = 1.5\ mm^2/s$ and $\sigma_f = 0.026\ N/m$.

3. Measurement techniques

Measuring the thickness of a moving wavy liquid film of less than a hundred microns is a challenging task. To achieve a high spatial and temporal resolution, a Laser Focus Displacement Meter (LFDM) according to [4] is applied for the film flow experiments. The measurement principle is based on focusing the light cone of a laser diode (wavelength $\lambda = 670\ nm$) onto the film surface. One of the focusing lenses is oscillated by electric excitation, shifting the spatial position of the focal point of the laser beam. At the gas-liquid interface, the beam is reflected to a great extent. For one cycle of oscillation an integrated photo detector receives through a pinhole the maximum amount of light in the time instant, when the focal point is directly located on the phase interface. The relation of the spatial position of the objective lens and the peak in light intensity allows to determine the distance of the film surface from the sensor. The sample frequency of the LFDM sensor is $f = 1.53\ kHz$. In order to reach the maximum temporal resolution to perform detailed measurements of the film structure, the analog output of the LFDM system has to be used. For this purpose, an external trigger unit was built to generate a suitable pulse for the AD-conversion board of the data acquisition computer. The range of the sensor is $0 \leq h < 0.6\ mm$ in air. The spatial resolution of $\delta h = 0.2\ \mu m$, specified by the manufacturer, is reduced by the AD-conversion to a value of $\delta h = 1\ \mu m$, which is still very accurate for the measurement of liquid films in the range of $20\ \mu m \leq h_f < 200\ \mu m$.

The air velocity measurements are performed via a 1-D LDV-system in backscattering mode through the transparent side walls. In order to measure the velocity close to the bottom of the indentation, the LDV probe is tilted by an angle of $\phi = 3\ ^\circ$. By the means of a short focal length of $f = 160\ mm$ and a beam expander, the spatial resolution in the direction normal to the wall is reduced to approximately $\delta y = 50\ \mu m$. This ensures a high resolution of the velocity profile inside the boundary layer. Due to the glass surface of the bottom of the duct and the tilt of the LDV probe, the measurement volume is reflected when the bottom of the dry duct is reached. This allows an accurate determination of $y = 0$, solving the common problem of the y-coordinate uncertainty in boundary layer measurements. For the LDV measurements the air flow is seeded with 1 μm oil droplets from an air assisted atomiser.

4. Determination of pressure gradient, shear-stress and sand-grain roughness

To achieve a high spatial resolution of the pressure gradient within the nozzle, the pressure gradient dp/dx is deduced from the velocity gradient du_{air}/dx along the main flow direction. Assuming that the the stream lines of the free stream close to the bottom wall are parallel to the surface, the pressure gradient is

$$\frac{dp}{dx} = -\frac{1}{\rho}\, u_{air}\, \frac{du_{air}}{dx} \tag{2}$$

A crucial parameter in the experimental study of liquid film motion is the driving shear-stress τ at the liquid/gas interface. Since the direct measurement of the shear-stress at the liquid/gas interface seems to be impossible, the shear-stress is deduced from the air velocity profiles above the liquid film.

Commonly, the air velocity profiles above a wall are matched to the logarithmic wall function [5], neglecting the wall roughness and assuming the absence of a pressure gradient. To deduce the shear-stress τ and the equivalent sand-grain roughness k_s from the air flow profile above the wavy film surface inside a nozzles, a modified boundary layer approach based on the assumption of van Driest is applied, introducing a damping function for the viscous sublayer according to Kays and Crawford [6–8].

The equation for the eddy viscosity ε_t

$$\frac{\varepsilon_t}{\nu} = \kappa^2 \left(y^+ + \delta y_0^+\right)^2 \left(1 - e^{-y^+/A^+}\right)^2 \left|\frac{\partial u^+}{\partial y^+}\right| \tag{3}$$

$$y^+ = \frac{y \cdot u_\tau}{\nu}, \quad u^+ = \frac{u}{u_\tau}, \quad u_\tau = \sqrt{\frac{\tau}{\rho}} \tag{4}$$

with the damping function $D = (1 - \exp(-y^+/A^+))$ allows with the parameters A^+ in the damping function D and δy_0^+ for fully rough walls a detailed description of the transition from the turbulent region of the boundary layer to the viscous sublayer. The effects of the wall roughness k_s and the pressure gradient dp/dx on the boundary layer are taken into account simultaneously [9]. After calculating the pressure gradient from the measured local velocity gradient, the input values k_s and τ of the modified boundary layer approach are varied until a best fit to the measured air velocity profile above the liquid film is achieved.

Disadvantage of this closure for the near wall region is that the equations have to be solved numerically. It is also limited in its use, if a very high favourable pressure gradient ($dp/dx < 0$) forces

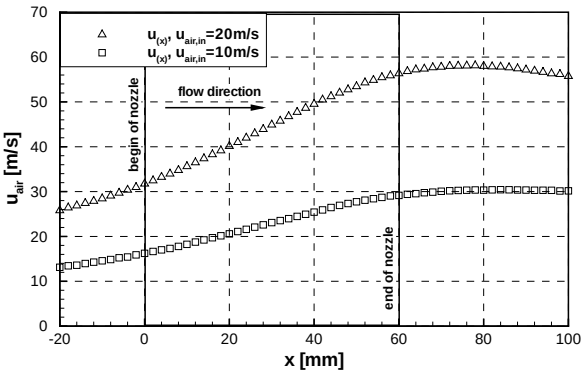

(a) Air velocity 1.5 *mm* above the film propagation surface

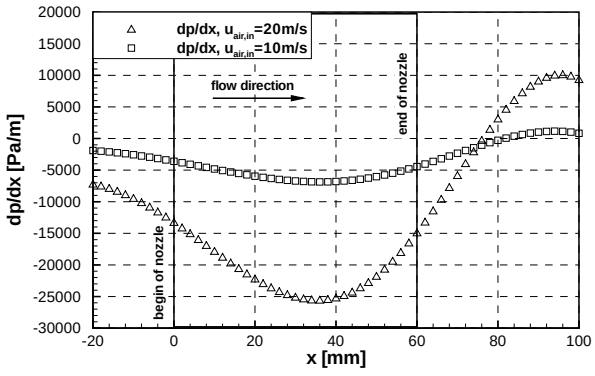

(b) Pressure gradient above the film propagation surface

Fig. 2 Air velocity and pressure gradient distribution in the test section

A^+ to very high values. In those cases, the viscous sublayer overwhelms the entire boundary layer, simply rendering the logarithmic wall function useless. This laminarisation minimises the data points which can be successfully fitted to the wall function.

5. Experimental Results

5.1. Results of film flow on a plane surface with dp/dx $\neq$ 0

According to the approach to separately investigate the effect of a pressure gradient on the liquid film flow, numerous experiments in the atmospheric wind tunnel have been performed. To deduce the shape factor Ψ (Eq. 1) for a certain film flow condition, various steps have to be undertaken.

In a first step the input parameters for solving the boundary layer equations of an accelerated air flow have to be identified. In addition to the static pressure and the air temperature, the local air velocity $u_{(x)}$ has to be determined to calculate the pressure gradient dp/dx. The pressure gradient is deduced from the velocity gradient of a stream line outside the boundary layer close to the wall. Figure 2(a) shows the air velocity $\bar{u}_{(x)}$ close to the propagation surface for the two investigated inlet conditions ($u_{air,\ in} = 10\ m/s$ and $u_{air,\ in} = 20\ m/s$) from $x = -30\ mm$ upstream to $x = 90\ mm$ downstream the front edge of the nozzle. Corresponding to the velocity gradient, the pressure gradient dp/dx within the nozzle can be calculated (Fig. 2(b)).

The further procedure to determine the equivalent sand-grain roughness and the shear-stress is shown exemplarily for a position in the middle of the nozzle at $x = 30\ mm$ in the following. Figure 3(a) shows the measured air velocity profile for an inlet air velocity of $u_{air,\ in} = 20\ m/s$ and a film load $\Lambda = 0.4\ cm^2/s$. The mirrored air velocity profile close to the film propagation surface is caused by the reflection of the tilted LDV probe volume at the air/liquid interface back into the main flow. The location of the sharp bend of the air velocity profile which could be observed in all measurements matches very well with the corresponding measured mean film thickness of $\bar{h}_f = 57\ \mu m$ in this case. With the information of the other input parameters, the modified boundary equation can be fitted to the air velocity profile above the liquid film by varying the values for the shear-stress τ and the equivalent sand-grain roughness k_s until the best fit is achieved (Fig. 3(b)).

Processing several measurements with different film loads Λ and $x = const.$ (Fig. 4(a)) yields normalised velocity profiles (Eq. 4) typical of the effect of the wall roughness k_s on the near wall

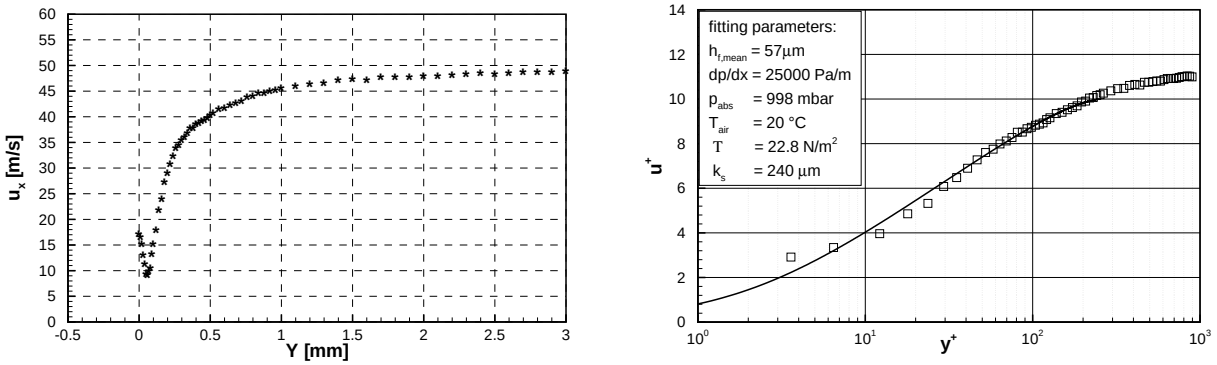

(a) Measured air velocity above the liquid film

(b) Fit of the boundary layer approach

Fig. 3 Determination of the shear stress and the equivalent sand-grain roughness $u_{air,\,in} = 20\ m/s$, $x = 30\ mm$, $\Lambda = 0.4\ cm^2/s$

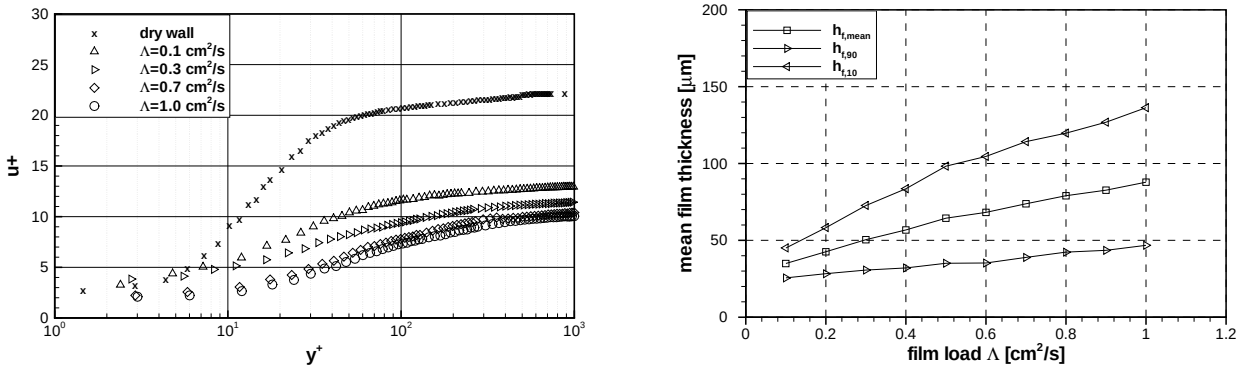

(a) Non-dimensional air velocity profiles, $u_{air,\,in} = 20\ m/s$

(b) Film thickness

Fig. 4 Air velocity and film thickness measurements at $x = 30mm$, $u_{air,\,in} = 20m/s$

velocity profiles, as it can be found in standard wall roughness investigations. Figure 5(a) shows the results of shear-stress τ and the equivalent sand-grain roughness k_s at the same position as in Fig. 4(a). The shear-stress τ increases first strongly compared to the dry wall, while a further increase of the film load Λ does not lead to significant higher shear-stress values. On the opposite the equivalent sand-grain roughness k_s increases continuously with the film load within the investigated range.

To finally calculate the shape factor Ψ according to Eq. 1, the mean film thickness has to be measured. Figure 4(b) shows the dependence of the mean film height $\bar{h}_f$ and a statistical value of the film height exceeded 10% ($h_{f,10}$) and 90% of the time ($h_{f,90}$) as a function of the film load. Typical of all results is the degressive increase of the film thickness as a function of the film load. This is caused by the enhanced transport of the film liquid with an increase of the film load as well as the film roughness. Compared to results from measurements on film flow with constant air velocity [10], the results of the film thickness measurements with an accelerated air flow tend to exhibit smaller film thicknesses at positions of comparable shear-stress. Applying the presented procedure to a large set of measurement conditions, a correlation for the shape factor Ψ

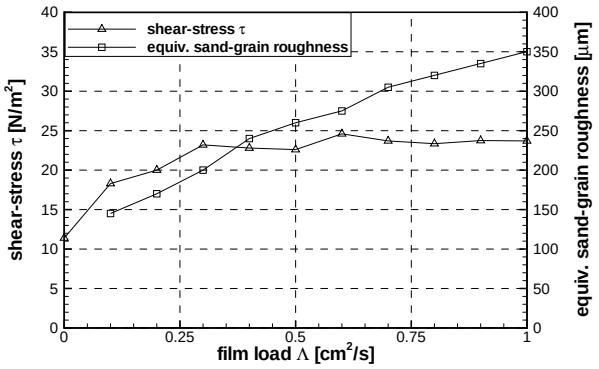

(a) Shear-stress and equivalent sand-grain roughness, $x = 30\ mm$, $u_{air,\ in} = 20 m/s$

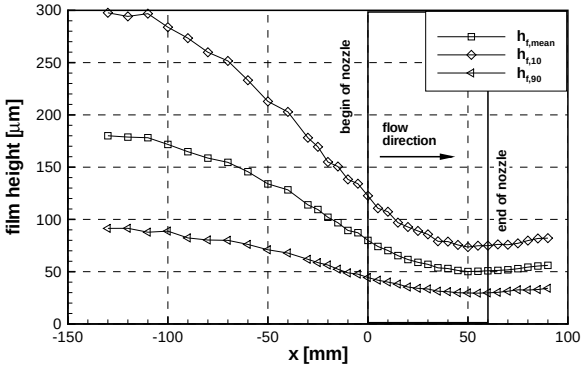

(b) Film thickness along the propagation surface, $\Lambda = 0.4\ cm^2/s$, $u_{air,\ in} = 20 m/s$

Fig. 5 Results of atmospheric experiments

with $We = \tau \cdot \bar{h}_f / \sigma_f$ and $On = \sqrt{\nu_f^2 \rho_f / (\sigma_f \bar{h}_f)}$ is deduced.

$$\Psi = We_f^{-0.035} \left(\frac{On_f}{On_{ref}} \right)^{0.07} \left(\frac{\sigma_f}{\sigma_{ref}} \right)^{-0.727} \cdot C, \quad C = \begin{cases} 0.77 & p^+ < -0.002 \\ 0.63 & p^+ \geq -0.002 \end{cases} \tag{5}$$

The film liquid properties in the Weber number and Ohnesorge number are referenced to the properties of water at $20°C$. One would expected, that the strong influence of the accelerated air flow onto the film dynamics is reduced when the acceleration parameter decreases, matching again the values for non-accelerated flow conditions. This can not be observed clearly in the present study. It seems that the presence of a notable negative pressure gradient leads to a non-equilibrium condition between the film motion and the air flow, comparable to the situation at the starting point of a liquid film. The air and film acceleration results in an enhanced momentum exchange. The resulting surface structure and, therefore, the roughness effect of the film surface does not change instantaneously according to the present shear-stress. In particular with regard to a similar effect at the starting point of a liquid film, the effect of an accelerated air flow onto the liquid film motion deserves a further closer attention.

To underline the importance of the consideration of the pressure gradient, the progress of the film thickness at a selected measurement condition of $u_{air,\ in} = 20\ m/s$ and $\Lambda = 0.4\ cm^2/s$ is plotted in Fig. 5(b). The point of the lowest film thickness (Fig. 5(b)) is upstream the point of the maximum air velocity (Fig. 2(a)), which is located downstream the nozzle. Since the film thickness is strongly influenced by the shear-stress and the pressure gradient, the film thickness values are the lowest for a location of both a high shear-stress τ and a strong negative pressure gradient dp/dx, which can be found inside the nozzle.

5.2. Results of film flow with dp/dx $\neq$ 0 and dΛ/dx $\neq$ 0

To proof the applicability of the correlation extracted from the experimental data of the atmospheric experiments described afore to film flow at elevated pressures with a varying local film load Λ_x, additional film flow experiments have been performed in the geometry described in Fig. 1(b)(top).

The comparison of the these film thickness measurement results with the numerical predictions

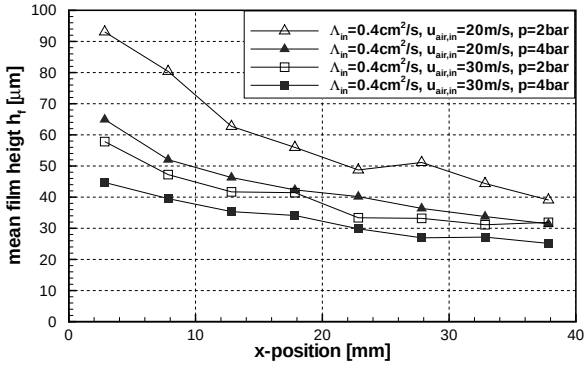

(a) Comparison of mean film thickness results

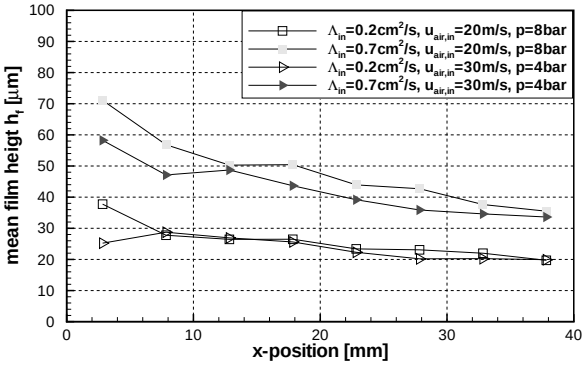

(b) Comparison of mean film thickness results

Fig. 6 Film thickness distribution in the 10°*nozzle*

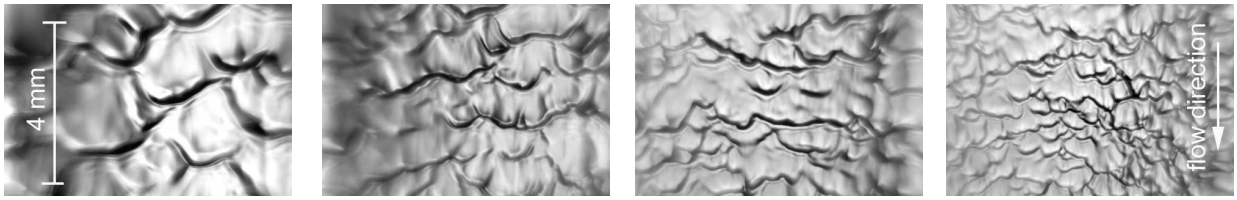

(a) $u_{air,\,in} = 20\ m/s$, $p = 2\ bar$

(b) $u_{air,\,in} = 30\ m/s$, $p = 2\ bar$

(c) $u_{air,\,in} = 20\ m/s$, $p = 4\ bar$

(d) $u_{air,\,in} = 30\ m/s$, $p = 4\ bar$

Fig. 7 Film Visualisation at $x = 20\ mm$, $\Lambda_{in} = 0.4\ cm^2/s$, flow top to bottom

[3] show a very good agreement. Figure 6(a) shows the mean film thickness $\bar{h}_f$ inside the nozzle for different air inlet velocities $u_{air,\,in}$ and air pressures. Assuming that the applied approach for predicting shear-driven liquid film flow can be extended to more complex flow conditions, points of similar shear-stress and pressure gradient should lead to similar film thickness results. According to $\tau \sim \rho \cdot u_{air}^2$, the results of the measurements at $u_{air,\,in} = 30\ m/s$ and $p = 2\ bar$ are indeed similar to the ones of $u_{air,\,in} = 20\ m/s$ and $p = 4\ bar$. The film flow visualisation in Fig. 7 shows the film surface structure $x = 20\ mm$ downstream the beginning of the nozzle the conditions in Fig. 6(a). While the visualisation of the film flow at $u_{air,\,in} = 20\ m/s$ and $p = 2\ bar$ (Fig. 7(a)) shows a larger smoother structure, the surface structure of $u_{air,\,in} = 30\ m/s$ and $p = 4\ bar$ (Fig. 7(d)) is considerably rougher, more and steeper waves appear. In opposite to that, the two images in the middle (Fig. 7(b) and Fig. 7(c) show similar surface structures, resulting in a comparable roughness effect on the air flow above the liquid film. This effect can be observed at all comparable positions, as shown exemplarily in Fig. 6(b) for different film loads and pressures.

6. Summary

Based on various experimental investigations of the liquid film flow motion with an accelerated co-current air flow at atmospheric pressure and temperature, a correlation for the effect of the wavy film surface on the gaseous phase has been developed. To achieve this results, the measured air velocity profiles above the liquid film were matched to a modified boundary layer approach, taking both the pressure gradient dp/dx and the equivalent wall roughness k_s into account simultaneously.

The results reveal, that the influence of a pressure gradient onto the film dynamics cannot be neglected. The results of high pressure experiments in a geometry typical of technical applications (e.g. airblast atomisers) allow the assumption, that the used approach can be applied to more complex geometries.

7. Acknowledgement

This work has been supported by a grant from the 'Competitive and Sustainable Growth Programme' of the European Community under contract GRD1-1999-10325 (CFD4C) which is gratefully acknowledged.

References

[1] Ebner, J., Schober, P., Schäfer, O., Koch, R. and Wittig, S. 2003 *Modelling of Shear-Driven Liquid Wall Films: Effect of Accelerated Air Flow on the Film Flow Propagation* International Journal "Progress in Computational Fluid Dynamics" (accepted, March 2003)

[2] Wurz, D. 1976 *Experimental Investigation Into the Flow Behaviour of Thin Water Films; Effect on a Cocurrent Air Flow of Moderate to High Supersonic Velocities: Pressure Distribution at the Surface of Rigid Wavy Reference Structures* Archiwum Mechaniki Stosowaney **28**(5-6), pp. 969 – 987

[3] Ebner, J., Schober, P., Schäfer, O. and Wittig, S. 2003 *Modelling of Shear-Driven Liquid Wall Films on Curved Surfaces: Effect of Accelerated Air Flow and Variable Film Load* Proceedings of the Ninth International Conference on Liquid Atomization and Spray Systems ICLASS, Sorrento, Italy

[4] Takamasa, T., Tamura, S. and Kobayashi, K. 1998 *Interfacial Waves on a Film Flowing Down Plate Wall in an Entry Region Measured with Laser Focus Displacement Meters* 3^{rd} International Conference on Multiphase Flow, Lyon, France, June 8 – 12

[5] Launder, B. and Spalding, D. 1974 *The Numerical Computation of Turbulent Flows* Computer Methods in Applied Mechanics and Engineering **3**, pp. 269 – 289

[6] van Driest, E. 1956 *On Turbulent Flow Near a Wall* Journal of the Aeronautical Science **8E1109/23**, pp. 1007 – 1012

[7] Kays, W. and Crawford, M. 1980 *Convective Heat and Mass Transfer* McGraw-Hill, New York

[8] Granville, P. 1985 *Mixing-Length Formulations for Turbulent Boundary Layers over Arbitrarily Rough Surfaces* Journal of Ship Research **29**(4), pp. 223 – 233

[9] Moffat, R. and Kays, W. 1984 *Advances in Heat Transfer - Review of Turbulent Boundary Layer Research* **16** Hartnett, J.P. and Irvine, T.F., Academic Press, Orlando

[10] Elsäßer, A., Samenfink, W., Ebner, J., Dullenkopf, K. and Wittig, S. 1997 *Dynamics of Shear-driven Liquid Films* Proceedings of the 7th International Conference on Laser Anemometrie - Advances and Applications, Karlsruhe, Germany, September 8 – 11